

Revision 1

The kinetic effect induced by variable cooling rate on the crystal-chemistry of spinel in basaltic systems revealed by EPMA mapping

Emanuela Gennaro¹, Gianluca Iezzi^{1,2}, Manuela Nazzari², Francesco Vetere³, Piergiorgio Scarlato²

Letizia Giuliani¹, Georg F. Zellmer⁴

(¹) Dipartimento di Ingegneria e Geologia (InGeO), Università degli Studi “G. d’Annunzio”, Chieti-Pescara, via dei Vestini 31, 66100 Chieti, Italy

(²) Istituto Nazionale di Geofisica e Vulcanologia, Sezione di Roma, via di Vigna Murata 605, 00143 Roma, Italy

(³) Dipartimento di Scienze Fisiche, della Terra e dell’Ambiente, Università degli Studi di Siena, Pian dei Mantellini 44, 53100, Siena, Italy

(⁴) Volcanic Risk Solutions, School of Agriculture and Environment, Massey University, Tennent Drive, Palmerston North 4410, New Zealand

ABSTRACT

The crystal-chemical variations of spinels grown as a function of cooling rate ($\Delta T/\Delta t$) were analyzed *via* X-ray electron-microprobe (EPMA) maps. Maps were collected serially by using a fixed distance. Spinels solidified from a tholeiitic MOR basaltic liquid (B₁₀₀) cooled at cooling rate ($\Delta T/\Delta t$) of 1, 7, 60 and 180 °C/h, between 1300 and 800 °C and at ambient P and fO_2 . As $\Delta T/\Delta t$ increases, the amount of spinel is invariably < 5 area% and its size decreases. Compared to the previous dataset

23 collected by common single and selected EPMA analytical points (112), the kinetic effects induced by
24 $\Delta T/\Delta t$ are here quantitatively captured by a large number of analyses (2052).

25 The TiO_2 , Al_2O_3 , MgO and FeO^{tot} show large compositional variations at low cooling rates (from
26 1 to 60 °C/h) and only the average TiO_2 concentration shows a well-defined trend as a function of $\Delta T/\Delta t$.
27 However, calculated average cation amounts (apfu) unveil quantitative kinetic effects. When $\Delta T/\Delta t$
28 increases (from 1 to 180 °C/h) only Ti^{4+} shows a linear decreasing trend, whereas the other major Al^{3+} ,
29 Fe^{3+} , Fe^{2+} and Mg^{2+} cations alone are scattered. Conversely, the sums of trivalent ($\text{Al}^{3+} + \text{Fe}^{3+}$) and
30 divalent ($\text{Mg}^{2+} + \text{Fe}^{2+}$) cations quantitatively capture the effect of the $\Delta T/\Delta t$. These new outcomes could
31 be the base of novel geospeedometers with significant implications in volcanology, geophysics and
32 material sciences in regard to silicate melt rheology on Earth. They should be extended to high pressure,
33 hydrated and low oxygen fugacity conditions. Further, the analytical approach used here to capture
34 kinetic effects on spinel growth and compositions can be also applied to other crystalline phases grown
35 from silicate liquids.

36
37 **Keywords:** spinel, crystal-chemistry, kinetic, cooling rate ($\Delta T/\Delta t$), EPMA maps

38 39 INTRODUCTION

40 Magnetite, ulvospinel, chromite and spinel *sensu stricto* are the most common minerals of the
41 spinel supergroup in magmatic rocks. They are almost ubiquitous in igneous rocks but occur in a
42 proportion of only few units of area% or vol% (e.g., Toplis and Carroll 1995; Jang et al. 2001; Freda et
43 al. 2008; Mollo et al., 2013, 2015; Xu et al., 2022; Keller et al., 2023). However, they can be found as
44 major mineral phases in several magmatic-hydrothermal ore deposits (e.g., Dare et al., 2014, 2015;
45 Nadoll et al., 2014; Chen et al., 2019). Minerals along the magnetite (Mt , $^{\text{T}}\text{Fe}^{3+\text{M}}\text{Fe}^{2+\text{M}}\text{Fe}^{3+}\text{O}_4$) and

46 ulvospinel (Usp , $\text{Fe}^{2+}\text{Mg}^{2+}\text{Ti}^{4+}\text{O}_4$) join, followed by the spinel sensu stricto (Sp s.s., $\text{Mg}^{2+}\text{Al}^{3+}_2\text{O}_4$)
47 are the most common non-aluminosilicate phases in igneous rocks (Deer et al., 1992; Bosi et al., 2019).

48 Many studies demonstrate that the crystal-chemistry of spinel-structured oxides (hereafter referred
49 as spinels) is able to reconstruct crystallization conditions, such as equilibrium (or dis-equilibrium)
50 growth, T , P and $f\text{O}_2$ of solidification (Ghiorso and Sack 1991; Toplis and Carroll 1995; Scaillet and
51 Evans 1999; Mollo et al., 2013; Coulthard et al., 2021; Keller et al., 2023). Experiments have also
52 highlighted that the crystal-chemistry of magmatic spinel depends on the chemical solidifying system
53 and crystallization of other silicate phases (Hammer, 2006; 2008; Iezzi et al., 2008, 2011; Mollo et al.,
54 2013; Mollo and Hammer, 2017; Giuliani et al., 2022). These studies highlight how solidification kinetics
55 can have a significant effect on the crystal-chemistry of spinels; the variation in kinetics has been largely
56 investigated as a function of variable cooling rate, i.e., $\Delta T/\Delta t$ (Hammer, 2008; Mollo et al., 2013; Mollo
57 and Hammer, 2017; Giuliani et al., 2022). Since the cooling conditions of a solidifying silicate liquid can
58 change by many orders of magnitude (Hammer, 2008; Giuliani et al., 2022), it is thus important to better
59 quantify its effect and, on the basis of the argument depicted above, to focus also on the crystal-chemistry
60 of spinels (Mollo et al., 2013; Giuliani et al., 2022), as already done for pyroxenes and plagioclases
61 (Muncill and Lasaga 1987; Lofgren et al. 2006; Hammer 2008; Iezzi et al. 2008, Mollo et al. 2010, 2011,
62 2012; Giuliani et al., 2022).

63 Until now, it is known that when $\Delta T/\Delta t$ increases the spinel sensu stricto molecule enriches and the
64 ulvospinel component decreases (Mollo et al., 2013; Giuliani et al., 2022). If not considered, these effects
65 may partially or totally invalidate the estimations of intensive parameters occurring during solidification
66 of magmas based on the crystal-chemistry of spinels (Ghiorso & Sack, 1991; Ishibashi, 2013; Mollo et
67 al., 2013; Arato & Audetat, 2015; Mollo et al., 2015; Pontesilli et al., 2019; Xu et al., 2022). Kinetic
68 effects on the crystal-chemistry of spinels are also extremely important because they impart the magnetic
69 properties of their host igneous rocks (O'Reilly, 1984; Banerjee, 1991; Pick and Tauxe 1994; Harrison

70 and Putnis, 1998; Zhou et al. 2000; Lattard et al., 2006; Bowles et al., 2011; Jackson & Bowles, 2014;
71 Alva-Valdivia et al., 2021; Dudzisz et al., 2022). Further, the crystal-chemical variations induced by
72 kinetics are potentially relevant for spinel-bearing ore deposits (Dare et al., 2012, 2014, 2015; Nadoll et
73 al., 2014; Canil et al., 2016; Zhao et al., 2018); similar to other crystalline phases, sluggish and rapid
74 solidification can enrich or deplete spinels with certain cations.

75 To refine and quantify the actual relationship between crystal-chemistry of spinels and cooling rate,
76 we re-investigated in this study some previous solidification experiments performed on a tholeiitic mid-
77 ocean ridge (MOR) basaltic system (labelled B₁₀₀). This initially superliquidus basalt was cooled at 1, 7,
78 60 and 180 °C/h down to 800 °C (Vetere et al., 2015; Giuliani et al., 2020). The compositions of spinels
79 in the four run-products were based on 112 single EPMA-WDS point analysis (Giuliani et al., 2022),
80 following the classical subjective selection of crystals. This classical routine approach has several
81 limitations that can mask the real relationship between crystal-chemistry and $\Delta T/\Delta t$, because: i) only
82 some crystals or parts of them are considered, ii) the number of analyzed crystals is limited and iii) the
83 selected crystals for analysis are poorly representative (Iezzi et al., 2014; Xu et al., 2022). These
84 limitations are here partially overcome by using X-ray electron-microprobe (EPMA) maps (Iezzi et al.,
85 2014; Higgins et al., 2021), allowing to collect thousands (2052) micro-chemical point analyses in a
86 serial way. The selected micro-chemical data unveil new and better-quantified relations between spinel
87 compositions and the kinetics of solidification. This analytical procedure and related outcomes are
88 uniquely able to capture the actual crystal-chemical variations recorded by crystals during their
89 crystallization.

90

91 **MATERIALS AND METHODS**

92 The syntheses of the four run-products considered here are described in detail by Vetere et al.
93 (2013, 2015). Briefly, the starting B₁₀₀ glass material was prepared through cycles (quenching, grinding,

94 heating) of melting at 1600 °C for several hours from a mid-ocean ridge tholeiitic basalt at known P and
95 fO_2 . The bulk composition of the sample is (wt%) SiO₂: 47.3(0.5), TiO₂: 1.0(0.0), Al₂O₃: 15.4(0.1),
96 FeO^{tot}: 10.2(0.0), MnO: 0.2(0.1), MgO: 9.4(0.2), CaO: 12.8(0.2), Na₂O: 1.9(0.1), K₂O: 0.1(0.0), while
97 H₂O is 53 ppm and the Fe²⁺/Fe^{tot} ratio is 0.386 (Vetere et al., 2015; Giuliani et al., 2022). The four run-
98 products were then solidified by loading about 50 mg of the B₁₀₀ glass into Pt tubes. Subsequently, the
99 sample charges were heated up to 1300 °C, kept at this temperature for 2 hours and then cooled down to
100 800 °C along four $\Delta T/\Delta t$ paths of 1 (~ 21 days), 7 (~ 3 days), 60 (~ 8 hours) and 180 (~ 3 hours) °C/h, at
101 air P and fO_2 . The chosen cooling rates were already discussed in former papers (Vetere et al., 2013;
102 2015), where the global crystallization behaviour of all crystalline phases was discussed. The quenched
103 charges were recovered, embedded in epoxy, ground flat, polished and carbon-coated for acquiring
104 micro-chemical maps at the HP-HT Laboratory of Experimental Volcanology and Geophysics of the
105 Istituto Nazionale di Geofisica e Vulcanologia in Roma (Italy).

106 The X-ray chemical EPMA-WDS maps were acquired by an electron probe micro-analyser JEOL-
107 JXA8200 combining EDS-WDS (equipped with five wavelength dispersive spectrometers with 12
108 crystals), following the same approach as reported by Iezzi et al. (2014). The selected representative
109 areas were designated on basis of previous textural characterizations (Giuliani et al., 2020). Each single
110 analytical point in the EPMA maps was acquired under vacuum using a focused electron beams with a
111 diameter of < 2 μm, an accelerating voltage of 15 kV and an electric current of 10 nA. The dwell time
112 per pixel was of 120 msec, for total acquisition times between 18 h 40 min and 22 h 33 min. X-ray
113 EPMA-WDS chemical maps were performed by stage rastering, keeping the electron beam stationary
114 while the stage moved. The collected EPMA point analyses were acquired with constant distances in
115 each run-product with resolution between 1 and 2 μm, on run-product portions with areas estimated
116 around 1 and 2 μm² (Table 1).

117 A linear off-peak correction was adopted, with each pixel scanned per element corresponding to a
118 full quantitative analysis, attained by correcting the intensity of each analytical point for background, k
119 factors and matrix effects. The used JEOL software permitted to export point analyses for each map on
120 basis of x-y coordinates. The reliability of chemical compositions obtained with EPMA maps was
121 checked by analyzing the same portion of 10 single spinels for each run-product using longer counting
122 times of 20 s on peak and 10 s on background, respectively, following the approach already reported in
123 Iezzi et al., (2014). Differences between these two analytical methods are less than 1 wt% for all oxides.
124 Thus, each point analysis or pixel of an EPMA map is a quantitative determination of the major oxide
125 components (Figure 1).

126 All EPMA-WDS single data points were first tabulated; then, only the point analyses with totals
127 comprising between 90 and 102 wt% were considered. The second screening was on the maximum
128 amounts of totally incompatible SiO₂, CaO, Na₂O and K₂O imposed to be < 2, < 1, < 2 and < 1 wt%,
129 respectively, whereas TiO₂, Al₂O₃, Fe₂O₃ and MgO contents were always accepted (Deer et al., 1992;
130 Mollo et al., 2013; Giuliani et al., 2022). The third step was the calculation of the cations (atom per
131 formula unit, apfu), ferric and ferrous speciation and molecules of spinels considering electric charge
132 neutrality, four oxygens, three cations and typical crystallographic site occupancy (Stormer, 1983).

133

134

RESULTS

135 The salient textural features of the four run-products are extensively discussed in Giuliani et al.
136 (2020) and are here shortly summarized. They are characterized by the solidification of plagioclase (plg),
137 clinopyroxene (cpx), spinel (sp) and glass (Table 1). As the cooling rate increases from 1 to 180 °C/h,
138 the run-products become progressively richer in cpx and poorer in plg, whereas the abundance of sp
139 accounts for < 5 area%; glass is present in significant abundance only at 180 °C/h. In parallel, the sizes
140 of crystals decrease, their number per area increases and their shapes switch from faceted to dendritic as

141 $\Delta T/\Delta t$ increases (Figure 1). These general features are here mirrored by the X-ray EPMA-WDS maps
142 displayed in Figure 1 for each oxide.

143 The number of selected analytical points of spinels decreases when the cooling rate increases due
144 to the reduction in size and number of crystals (Figure 1). At 180 °C/h only one spinel crystal with a
145 suitable size (~ 20 μm) was available (Figure 1). The average oxide compositions and related variations
146 are displayed in Table 2, while the abundance of their major oxides (wt%) are shown in Figure 2, where
147 the TiO_2 , Al_2O_3 , MgO and MnO contents are plotted against FeO^{tot} . The final and reliable analytical
148 points of each spinel crystal per run-product are reported in Tables S1a-d. At low $\Delta T/\Delta t$, the significant
149 variations around average contents (Table 2) reflect the high compositional zonation of single spinel
150 crystals (Figure 2). The highest oxide content in these synthetic spinels is invariably FeO^{tot} , ranging
151 between 62-90 wt%; the FeO^{tot} range shifts towards 62 wt% when $\Delta T/\Delta t$ increases from 1 to 180 °C/h
152 (Figure 2). The ranges of MgO , Al_2O_3 and TiO_2 oxides tend to decrease when the cooling rates increases.
153 They are extremely variable at 1 and 7 °C/h, with ranges up to 17, 15 and 17 wt% respectively (Figure
154 2). By contrast, these oxides show only limited variations at 180 °C/h (Figure 2). The MnO ranges are
155 relatively limited due to its absolute low content in the B_{100} system (Figure 2). Overall, MgO and Al_2O_3
156 augment and TiO_2 decreases as $\Delta T/\Delta t$ changes from 1 to 180 °C/h (Figure 2), while at 1 and 7 °C/h MgO ,
157 Al_2O_3 and TiO_2 display clustered compositions (Figure 2). The contents of TiO_2 and Al_2O_3 shift towards
158 the bulk chemical B_{100} composition (see above) as $\Delta T/\Delta t$ increases from 1 to 180 °C/h (Figure 2).

159 The trends depicted by oxides are mirrored by calculated cations (Figure 3). The content of Mn^{2+}
160 is invariably < 0.1 apfu, while Mg^{2+} , Al^{3+} and Ti^{4+} are < 1 , < 0.7 and < 0.5 apfu, respectively; the ranges
161 of Fe^{2+} and Fe^{3+} are between 0.2-1.4 and 1-2 apfu, respectively (Figure 3). Again, at 1 and 7 °C/h Mg ,
162 Fe^{2+} , Fe^{3+} and to a lesser extent Al^{3+} display clustering and large apfu variations, whereas Ti^{4+} follows
163 an almost linear decreasing trend when Fe^{3+} increases (Figure 3). Overall, the increasing of Fe^{3+} is linked
164 to the depletion depletion in Fe^{2+} and enrichments of Mg^{2+} and Al^{3+} (Figure 3). Hence, an increase of

165 Fe^{3+} favors a depletion of the Usp and an enrichment of the spinel sensu stricto components (Figure 3,
166 Table 2).

167 The presence of clustering of cation abundances requires an analysis of their frequencies. The
168 variations of Mg^{2+} and Ti^{4+} cations were divided in ten classes, while those of Fe^{2+} , Fe^{3+} and Al^{3+} in
169 twenty classes, each encompassing 0.1 apfu (Figure 4). An increase of the cooling rate results in a
170 progressive depletion of Ti^{4+} from 0.4-0.1 down to 0.1 apfu, the most abundant Al^{3+} content changes
171 from 0.1 to 0.4 apfu and the Fe^{3+} maximum moves from about 1.8 down to 1.5-1.6 apfu (Figure 4). The
172 two divalent Mg^{2+} and Fe^{2+} cations display a bimodal distribution at 1°C/h , becoming unimodal for the
173 other three run-products. The maximum content of Fe^{2+} first decreases, then increases and again
174 decreases when $\Delta T/\Delta t$ changes from 7 through 60 to 180°C/h , whereas Mg^{2+} displays an opposite
175 behavior (Figure 4).

176 The synthetic spinel crystals grown in the four experimental charges can be rigorously classified
177 following the recent scheme reported in Bosi et al. (2019). All these spinels have ΣR^{3+} ($= \text{Cr}^{3+} + \text{Fe}^{3+} + \text{Al}^{3+}$)
178 > 1.0 apfu and the $\Sigma R^{3+}/R^{2+}$ ratio is between $2/3$ and 2 , so they belong to the 2-3 spinel subgroup
179 ($\text{A}^{2+}\text{B}^{3+}\text{O}_4$). The by far dominant B-cation is Fe^{3+} , whereas dominant A-cations are Fe^{2+} and Mg^{2+} as a
180 function of run-products and crystals (Tables 2 and S1, Figures 3 and 4). Therefore, these spinels are
181 either magnetite or magnesioferrite. However, in petrological studies, such discrimination of the
182 dominant A-cation is rarely considered and the Fe^{3+} -rich spinels are referred to as magnetite (Stormer,
183 1983; Mollo et al., 2013). Following the common classification of spinels in magmatic rocks, they are
184 classified according to the magnetite [Mt , ${}^{\text{T}}\text{Fe}^{3+\text{M}}(\text{Fe}^{2+}\text{Fe}^{3+})\text{O}_4$], spinel sensu stricto [Sp s.s.,
185 ${}^{\text{T}}\text{Mg}^{2+\text{M}}\text{Al}^{3+}_2\text{O}_4$] and ulvospinel [Usp , ${}^{\text{T}}\text{Fe}^{2+\text{M}}(\text{Fe}^{2+}\text{Ti}^{4+})\text{O}_4$] molecular end-members (Table 2). Their
186 average compositions are plotted in Figure 5.

187

188

DISCUSSION

189 The average oxide, cation and molecular compositions of the same spinel crystals analyzed by a
190 classical set of single EPMA analytical points (Giuliani et al., 2022) and those attained here by serial
191 points from EPMA maps are different (Figure 5). Such differences can be related only to the subjective
192 selection of analyzed crystals, as well as to the relative low number of single EPMA analytical points
193 when compared to maps, i.e., 112 vs. 2052 (Iezzi et al., 2014). However, the companion study conducted
194 with the classical selection of single EPMA analytical points already highlighted that average Al_2O_3
195 qualitatively increases, FeO^{tot} and TiO_2 both decreased, whilst spinel sensu stricto increases as the
196 cooling rates increased (Giuliani et al., 2022). In summary, the average oxide, cation and/or molecular
197 compositions of solidified spinels were apparently only in part able to capture the kinetic of solidification
198 induced by $\Delta T/\Delta t$ experimental rates (Figures 2, 3, 4 and Table 2).

199 The X-ray EPMA-WDS maps provide the micro-chemical characterizations of a large and
200 systematic number of spinel crystals and related portions. These spinels, cooled from the same bulk
201 anhydrous silicate liquid at room P and redox state, follow quantitative trends, never reported before.
202 The variations of mean values of single cations vs. $\Delta T/\Delta t$ indicates that only Ti^{4+} follows a very well
203 defined trend ($R^2 = 0.94$) in agreement with the previous finding reported in Giuliani et al. (2022),
204 whereas Al^{3+} is relatively poorly defined ($R^2 = 0.67$, Figure 6) (only a qualitative evolution trend was
205 observed in Giuliani et al., 2002). By contrast, Fe^{3+} , Fe^{2+} and Mg^{2+} display scattered evolution trends as
206 a function of $\Delta T/\Delta t$, with different average values from those previously determined. Further, their
207 average values differ from those previously determined by single EPMA analytical points (Figure 6).
208 These apparently absent relationships between each trivalent and divalent cations with respect to cooling
209 conditions is overcome when considering their sums, i.e. $\text{Al}^{3+} + \text{Fe}^{3+}$ and $\text{Mg}^{2+} + \text{Fe}^{2+}$. In fact, their
210 average apfu highly and linearly correlate ($R^2 = 0.96$ and 0.92) with $\Delta T/\Delta t$ (Figure 6). From a molecular
211 view, the magnetite pole is clearly the most abundant in all run products. However, when $\Delta T/\Delta t$ increases,
212 the ideal magnetite pole, on average, slightly decreases, the spinel sensu stricto, strongly increases and

213 the ulvospinel end-member decreases in response to the significant depletion of Ti^{4+} (Table 2 and Figure
214 7). These trends quantitatively complement and modify the results reported in previous experimental
215 investigations (Mollo et al., 2013; Pontesilli et al., 2019; Giuliani et al., 2022).

216 The linear relationships between crystal-chemical formulas and cooling rate represent a
217 geospeedometer based on spinel-structured oxides at ambient P and $f\text{O}_2$. The corollary of these outcomes
218 is that the crystal-chemical variations of spinel in basaltic liquids can be entirely captured only if the sum
219 of tetra-, tri- and di-valent cations are considered, as shown in Figure 7. It is also worth noting that only
220 TiO_2 or Ti^{4+} is able to track the effect of $\Delta T/\Delta t$ since the other cations recognize the effect of kinetics
221 only if considering trivalent and divalent cations together (Figure 6). In line, the observed large variations
222 (standard deviations) of crystal-chemical features of spinels especially at low cooling rates (Table 2)
223 reflect their evolution, i.e. zonation of crystals and multiple crystallization events, in response to
224 progressive crystallization. All these considerations can be extended to other mineral species and can be
225 captured only by using serial EPMA point analytical procedures, as shown for plagioclase by Iezzi et al.
226 (2014) and Higgins et al. (2021). Other reinvestigations following this procedure may be able to decipher
227 the actual absence of significant trends between crystal-chemistry of phases and kinetics.

228 Based on textures of solidified crystals and thermodynamic estimations performed on
229 clinopyroxenes and plagioclases, spinel was interpreted to be one of the first phases to precipitate,
230 followed by chain-silicates and finally feldspars (Vetere et al., 2013, 2015; Giuliani et al., 2020, 2022).
231 This interpretation is further corroborated here by the very high linear variations of Ti^{4+} , $\text{Al}^{3+} + \text{Fe}^{3+}$ and
232 $\text{Mg}^{2+} + \text{Fe}^{2+}$ induced through changes in $\Delta T/\Delta t$ (Figures 6 and 7). Indeed, such variations can be achieved
233 only if the silicate liquid composition (B_{100}) from which spinel precipitates is constant. Starting from this
234 point, it is possible to explain the depicted behavior displayed by cations as a function of kinetics in the
235 light of nucleation and crystal growth. Below the liquidus temperature and among thermodynamic stable

236 phases, dynamic solidification favors the nucleation of phases with the lowest energetic barriers of
237 formation (Kirkpatrick, 1983, Lasaga, 1998, Iezzi et al., 2008, Zhang, 2008).

238 This qualitative principle is now relatively well established for silicate crystalline phases grown
239 from natural and chemically complex silicate liquids (Iezzi et al., 2009, 2011). First, it explains that Fe-
240 rich phases like spinel are more rapidly nucleated than silicates like clinopyroxenes and plagioclases.
241 Second, it also furnishes an explanation for the evolution of crystal-chemical formulas of spinels (Figures
242 6 and 7). The formation of stable nuclei is attained by random compositional fluctuations of molecular
243 units in the melt below the liquidus temperature (Lasaga, 1998, Zhang, 2008). The probabilistic
244 compositional fluctuations involve the continuous breaking and formation of chemical bonds; however,
245 strong chemical bonds have a more limited compositional space to explore, i.e., a limited compositional
246 difference between the initial liquid and the final structural arrangement (Roskosz et al., 2005, 2006;
247 Iezzi et al., 2014). Hence, the energetic barrier of nucleation scales with the number and strength of
248 chemical bonds of cations with oxygens.

249 Spinel solidified in this system incorporate Ti^{4+} , Al^{3+} , Fe^{3+} , Mg^{2+} and Fe^{2+} (Figures 6 and 7).
250 Indeed, the strongest bonds are those between Ti^{4+} and O^{2-} , followed by those of Al^{3+} and Fe^{3+} and finally
251 of Mg^{2+} and Fe^{2+} with oxygens (Pauling, 1960; Kirkpatrick, 1983; Dingwell, 2006). In light of these
252 considerations, the increase in cooling rate progressively disadvantages the incorporation of Ti^{4+} (Figures
253 4, 6 and 7). At low rates, TiO_2 incorporation spans very broad chemical composition variations, but at
254 $180\text{ }^\circ\text{C/h}$ its amount is very close to that of the starting silicate liquid (Figure 2). The incorporation of
255 progressively lower amounts of Ti^{4+} and the electric charge neutrality then drive up the amounts of
256 trivalent and divalent cations. Since the incorporation of Ti^{4+} is reduced, divalent cations follow the same
257 trend and the trivalent cations are introduced to compensate their decrease (Figures 6 and 7). This further
258 explains the poor preference between the two trivalent and divalent cations in the crystallized spinels.

259 Although SpinMelt-2.0 (Nikolaev et al., 2018a, 2018b) is the most recently developed suite for
260 calculating the theoretical crystal-chemical formula of spinel at equilibrium with its liquid, it is not
261 suitable for the B₁₀₀ experimental material synthesized in this his study, since the bulk composition of
262 B₁₀₀ is practically Cr-free and solidification occurred at too high fO_2 . In turn, the calculated equilibrium
263 composition was obtained via alphasmelts 1.9 (Asimow and Ghiorso, 1998; Ghiorso et al., 2002; Smith
264 and Asimow, 2005; Giuliani et al., 2022) at ambient P and at redox conditions as high as possible (i.e.,
265 QFM + 2.5). This theoretical composition is $Ti_{0.52}Fe^{3+}_{0.78}Al_{0.17}Fe^{2+}_{1.23}Mg_{0.29}O_4$ and differs even from the
266 average spinel $Ti_{0.12}Fe^{3+}_{1.62}Al_{0.12}Fe^{2+}_{0.71}Mg_{0.40}O_4$ grown at 1°C/h (Table 2). When compared with the
267 ideal equilibrium spinel, the experimental one is strongly depleted in Ti^{4+} and Fe^{2+} and highly enriched
268 in Fe^{3+} (Figure 3). The increased rate of cooling exacerbates these differences since at 180 °C/h the
269 average spinel is $Ti_{0.01}Fe^{3+}_{1.57}Al_{0.37}Fe^{2+}_{0.35}Mg_{0.66}O_4$ (Table 2 and Figure 3). It is also important to
270 consider that the average ratio of ferrous vs. ferric follows a scattered trend with respect to $\Delta T/\Delta t$ (Table
271 2). All these differences between theoretical thermodynamic and observed kinetic compositions, if not
272 considered, can alter the reconstruction of crystallization conditions. Similarly, low amounts of Ti^{4+}
273 could be misinterpreted to derive from entrainment of foreign spinel crystals (xenocrystals) into the host
274 magmas.

275 276 **IMPLICATIONS AND CONCLUSIONS**

277 In this study, we report the chemical compositions of spinels, experimentally synthesized from
278 basaltic liquid at different cooling rate, as obtained from EPMA maps. The increase of cooling rate (from
279 1 to 180 °C/h) strongly influences the cations distribution between the melt and the crystallized phases.
280 Spinel enriches continually in Al^{3+} and depletes in Ti^{4+} , therefore spinel sensu stricto is favored at higher
281 cooling rate with respect to ulvospinel and magnetite components. The linear relationships between the
282 crystal-chemical formulas (especially for Ti^{4+} , $Mg^{2+} + Fe^{2+}$ and $Al^{3+} + Fe^{3+}$ sums) and cooling rate are at

283 the base of a novel geospeedometer for spinels at ambient P and fO_2 . Actually, the experimental
284 conditions considered in this study are directly relevant for natural basaltic liquids (aphyric or residual
285 melts, McCarthy et al., 2023) after their eruptions and emplacements under subaerial and submarine
286 conditions. The fO_2 calculated for our experimental spinels using the oxybarometer of Arato and Audédat
287 (2017) computes high redox conditions such as ΔQFM of +2 for $\Delta T/\Delta t$ of 1 and 7 °C/h, and +4 and +8
288 respectively for spinels produced at 60 and 180 °C/h; these estimations are in line with those already
289 estimated in Giuliani et al. (2022) and more importantly several MORBs are now considered to be
290 emplaced at fO_2 close to QFM (Cottrell et al., 2021).

291 The range in cooling conditions of 1, 7, 60 and 180 °C/h occurs in natural MORB lavas and magmas
292 in response to thermal contrasts between silicate liquid and the surrounding environment, such as wall-
293 rocks, water, air as well as based on the volume and thickness of the solidifying melt or magma (Vetere
294 et al., 2015; Lanzafame et al., 2017; Giuliani et al., 2022). Previous numerical simulations indicate that
295 cooling rates of 1 and 7 °C/h can develop in the innermost portions of B₁₀₀-like lavas with a thickness of
296 a few meters, whereas 60 and 180 °C/h are typical for outermost portions of meter-thick lavas or in
297 central parts of dm-thick lavas and bombs (Vetere et al., 2015; Giuliani et al., 2022; McCarthy et al.,
298 2023). Spinel crystals crystallize early and have a high density with respect to silicate melts (about 5000 vs.
299 2600 kg/m³, respectively). According to Giordano et al (2008) viscosity model and utilizing the Stokes
300 law as for the falling sphere viscometry (Vetere et al., 2006) as temperature goes from 1350 to 1200 °C,
301 B₁₀₀ (MORB) viscosity ranges between 2 and 16 Pa*s. Under these conditions, a crystal with a size of
302 0.1 mm can fall with a velocity ranging from 2.77 *10⁻⁵ m/s (high T) and covering a sinking distance of
303 2.4 m in 1 day or 2.77 *10⁻⁶ but in this case the falling distance is only 24 cm.

304 Finally, it must be noted that the very low amount of spinels (< 5 area% Giuliani et al., 2022) at
305 the beginning of the crystallization path do not significantly impact on the rheology of the entire

306 suspension (Vetere et al., 2022). At the same time, this low amount is only able to changes the Fe content
307 in the residual melt. Our system is almost anhydrous and, as SEM proved, tiny bubbles are absent.

308 In turn, spinels crystallized at different cooling conditions (with different crystal-chemistries) at
309 variable thicknesses into a silicate liquid (lavas, dykes, etc.) can accumulate at similar levels and mimic
310 disequilibrium crystal assemblages. By contrast, if crystallized spinels remain at the positions where
311 different cooling rates develop, the crystal-chemical variations will be indicative of cooling regimes they
312 experienced. Such a scenario has been observed for pillow basalts, dykes and lavas (Zhou et al., 2000;
313 Kissell et al., 2010; Mollo et al., 2011; McCarthy et al., 2023). In pillow basalts the very thin carapace
314 hosts tiny, Fe-rich and Ti-poor spinels, whereas moving towards the innermost parts the spinel increases
315 its size and the amount of Ti (Zhou et al., 2000) in line with the textural (Giuliani et al., 2020) and
316 chemical trends unveiled here (Figures 6 and 7).

317 The changes of cations in spinels induced by cooling affect their magnetic properties (Harrison and
318 Putnis, 1996, 1998; Lattard et al., 2006; Chadima et al., 2009) and agree with magnetic variations
319 observed in basaltic dikes with progressive reduction of cooling conditions from external to internal parts
320 (Smith and Prévot, 1977). Again, these results can be captured only by the use of X-ray EPMA maps and
321 understood using the linear cation variations reported here (Figures 6 and 7).

322 The preference of element incorporations in spinel as a function of $\Delta T/\Delta t$ is also useful to
323 concentrate in them toxic or critical elements from waste (Zhao et al., 2017). Cations with affinities with
324 Ti^{4+} , Al^{3+} , Fe^{3+} , Fe^{2+} and Mg^{2+} can be preferentially enriched (or depleted) in spinels during
325 crystallization as a function of cooling dynamics only, i.e., by modulating the thickness of the melt or
326 the temperature of its environment. Since the incorporation of tetravalent (Ti^{4+}) and divalent is reduced
327 upon the increase of the cooling rate, trivalent cations are introduced, enriching spinel in minor and trace
328 trivalent elements as Cr and REE.

329

330

Acknowledgements

331 This study was funded by the PRIN (2009PZ47NA_003) project “Time Scales of Solidification in
332 Magmas: Application to Volcanic Eruptions, Silicate Melts, Glasses, Glass-Ceramics” awarded to G.
333 Iezzi. Most of this study was conducted during the post-doc of E. Gennaro.
334 We would like to thank the editors and the reviewers for their thorough and constructive comments,
335 which helped to improve this manuscript.

336

337

REFERENCES

- 338 Alva-Valdivia, L.M., Vidal-Solano, J.R., Velderrain-Rojas, L.A., and Gonzalez-Rangel J.A.
339 (2021) Rock magnetic characterization and paleomagnetic directional analysis of Isla San Pedro Nolasco
340 dikes, Gulf of California, Mexico. *Bulletin of Volcanology* 83, 52. [https://doi.org/10.1007/s00445-021-](https://doi.org/10.1007/s00445-021-01477-w)
341 [01477-w](https://doi.org/10.1007/s00445-021-01477-w).
- 342 Arató, R., and Audétat, A. (2017) FeTiMM – A new oxybarometer for mafic to felsic magmas.
343 *Geochemical Perspectives Letters* 5, 19–23. <https://doi.org/10.7185/geochemlet.1740>.
- 344 Asimow, P.D., and Ghiorso, M.S. (1998) Algorithmic modifications extending MELTS to
345 calculate subsolidus phase relations. *American Mineralogist* 83, 1127–1132.
- 346 Banerjee, S.K. (1991) Magnetic properties of Fe-Ti oxides. In: Lindsley DH (ed) *Oxide Minerals:*
347 *petrologic and magnetic significance. Reviews in Mineralogy*, vol 25. Mineralogical Society of America,
348 Chantilly, VA, pp 107–128.
- 349 Bosi, F., Biagioni, C. and Pasero, M. (2019) Nomenclature and classification of the spinel
350 supergroup. *European Journal of Mineralogy*, 31, 183–192.
- 351 Bowles, J.A., Gee, J.S., Burgess, K., and Cooper, R.F. (2011) Timing of magnetite formation in
352 basaltic glass: insights from synthetic analogs and relevance for geomagnetic paleointensity analyses.
353 *Geochemistry, Geophysics, Geosystems* 12(2):1–18.

354 Canil, D., Grondahl, C., Lacourse, T., and Pisiak, L.K. (2016) Trace elements in magnetite from
355 porphyry Cu–Mo–Au deposits in British Columbia, Canada. *Ore Geology Reviews*, Volume 72, Part 1,
356 Pages 1116-1128.

357 Chadima, M., Cajz, V., and Tycova, P. (2009) On the interpretation of normal and inverse magnetic
358 fabric in dikes: examples from the Eger Graben, NW Bohemian Massif. *Tectonophysics* 466(1–2):47–
359 63.

360 Chen, W., Yinga, Y.-C., Baia, T., Zhanga, J.-J., Jianga, S.-Y., Zhaoa, K.-D., Shinb, D., and
361 Kynicky, J. (2019) In situ major and trace element analysis of magnetite from carbonatite-related
362 complexes: Implications for petrogenesis and ore genesis. *Ore Geology Reviews* 107 (2019) 30–40.

363 Cottrell, E., Birner, S., Brounce, M., Davis, F.A., Waters, L.E., Kelley, K.A., 2021. Oxygen
364 fugacity across tectonic settings. In: *AGU Geophysical Monograph Series Redox Variables and*
365 *Mechanisms in Magmatism and Volcanism*. Editors: Neuville, D. R. and Moretti, R. Wiley.
366 <https://doi.org/10.1002/9781119473206.ch3>

367 Coulthard Jr, D.A., Zellmer, G.F., Tomiya, A., Jégo, S., and Brahm, R. (2021) Petrogenetic
368 implications of chromite-seeded boninite crystallization experiments: Providing a basis for chromite-
369 melt diffusion chronometry in an oxybarometric context. *Geochimica et Cosmochimica Acta* 297, 179–
370 202.

371 Dare, S.A.S., Barnes, S.-J., and Beaudoin, G. (2012) Variation in trace element content of magnetite
372 crystallized from a fractionating sulfide liquid, Sudbury, Canada: implications for provenance
373 discrimination. *Geochimica et Cosmochimica Acta* 88:27–50. doi:10.1016/j.gca.2012.04.032.

374 Dare, S.A.S., Barnes, S.-J., Beaudoin, G., Méric, J., Boutroy, E., and Potvin-Doucet, C. (2014)
375 Trace elements in magnetite as petrogenetic indicators. *Mineralium Deposita* 49, 785–796.

376 Dare, S.A.S., Barnes, S.-J., and Beaudoin, G. (2015) Did the massive magnetite ‘lava flows’ of El
377 Laco (Chile) form by magmatic or hydrothermal processes? New constraints from magnetite
378 composition. *Mineralium Deposita* 50, 607-617.

379 Deer, W.A., Howie, R.A., and Zussmann, J. (1992) An introduction to the rock-forming minerals.
380 – 2nd edition. Longman, Harlow, 696 pp.

381 Dingwell, D.B. (2006) Transport properties of magmas: diffusion and rheology. *Elements* 2, 281–
382 286.

383 Dudzisz, K., Kontny, A., and Alva-Valdivia, L.M. (2022) Curie temperatures and emplacement
384 conditions of pyroclastic deposits from Popocatepetl volcano, Mexico. *Geochemistry, Geophysics,*
385 *Geosystems*, 23, e2022GC010340. <https://doi.org/10.1029/2022GC010340>.

386 Freda, C., Gaeta, M., Misiti, V., Mollo, S., Dolfi, D., and Scarlato, P. (2008) Magma–carbonate
387 interaction: an experimental study on ultrapotassic rocks from Alban Hills (Central Italy). *Lithos*
388 101:397–415.

389 Ghiorso, M.S., and Sack, R.O. (1991) Fe-Ti oxide geothermometry: thermodynamic formulation
390 and the estimation of intensive variables in silicic magmas. *Contributions to Mineralogy and Petrology*
391 108:485–510.

392 Ghiorso, M.S., Hirschmann, M.M., Reiners, P.W., and Kress, V.C. (2002) The pMELTS: a revision
393 of MELTS for improved calculation of phase relations and major element partitioning related to partial
394 melting of the mantle to 3 GPa. *Geochemistry, Geophysics, Geosystems* 3, 1030.

395 Giordano, D., Russell, J. K., and Dingwell, D. B. (2008). Viscosity of magmatic liquids: a model.
396 *Earth Planet. Sci. Lett.*, 271, 123–134.

397 Giuliani, L., Iezzi, G., Vetere, F., Behrens, H., Mollo, S., Cauti, F., Ventura, G., and Scarlato, P.
398 (2020) Evolution of textures, crystal size distributions and growth rates of plagioclase, clinopyroxene

399 and spinel solidified at variable cooling rates from a mid-ocean ridge basaltic liquid. *Earth-Science*
400 *Reviews* 204, 103165.

401 Giuliani, L., Vetere, F., Iezzi, G., Nazzari, M., Mollo, S., Behrens, H., Scarlato, P., and Ventura,
402 G. (2022) Crystal-chemical variations of spinel, clinopyroxene, and plagioclase in MORB basaltic melt
403 induced by continuous cooling. *Chemical Geology* 594, 120765.

404 Hammer, J.E. (2006) Influence of fO_2 and cooling rate on the kinetics and energetics of Fe-rich
405 basalt crystallization. *Earth and Planetary Science Letters* 248:618–637.

406 Hammer, J.E. (2008) Experimental studies of the kinetics and energetics of magma crystallization.
407 In: Putirka KD, Tepley FJ (ed) *Minerals, inclusions and volcanic processes*. *Reviews in Mineralogy and*
408 *Geochemistry*, vol 69. Mineralogical Society of America, Chantilly, VA, pp 9–59.

409 Harrison, R.J., and Putnis, A. (1996) Magnetic properties of the magnetite-spinel solid solution:
410 Curie temperatures, magnetic susceptibilities and cation ordering', *American Mineralogist* 81, 375–384.

411 Harrison, R.J., and Putnis, A. (1998) The Magnetic Properties and Crystal Chemistry of Oxide
412 Spinel Solid Solutions. *Surveys in Geophysics* 19, 461–520. <https://doi.org/10.1023/A:1006535023784>.

413 Heap, M.J., Baud, P., Meredith, G., Vinciguerra, S., Bell, A.F., and Main, I.G. (2011) Brittle creep
414 in basalt and its application to time-dependent volcano deformation. *Earth and Planetary Science Letters*
415 307:71–82.

416 Higgins, O., Sheldrake, T., and Caricchi, L. (2021) Quantitative chemical mapping of plagioclase
417 as a tool for the interpretation of volcanic stratigraphy: an example from Saint Kitts, Lesser Antilles.
418 *Bulletin of Volcanology*, 83, 51, <https://doi.org/10.1007/s00445-021-01476-x>.

419 Iezzi, G., Mollo, S., Ventura, G., Cavallo, A., and Romano, C. (2008) Experimental solidification
420 of anhydrous latitic and trachytic melts at different cooling rates: the role of nucleation kinetics. *Chemical*
421 *Geology* 253:91–101.

422 Iezzi, G., Mollo, S., and Ventura, G. (2009) Solidification behavior of natural silicate melts and
423 volcanological implications. In N., Lewis, A. Moretti, (Eds.), *Volcanoes: Formation, Eruptions and*
424 *Modeling*. Nova publishers, New York, pp. 127–151.

425 Iezzi, G., Mollo, S., Torresi, G., Ventura, G., Cavallo, A., and Scarlato, P. (2011) Experimental
426 solidification of an andesitic melt by cooling. *Chemical Geology*, 283:261–273.

427 Iezzi, G., Mollo, S., Shahini, E., Cavallo, A., and Scarlato, P. (2014) Investigating Petrologic
428 indicators of Magmatic Processes in Volcanic Rocks, The cooling kinetics of plagioclase feldspar as
429 revealed by electron-microprobe mapping. *American Mineralogist*, Volume 99, pages 898–907.

430 Ishibashi, H. (2013) Spinel–melt oxygen barometry: a method and application to Cenozoic alkali
431 basaltic magmas from the Higashi–Matsuura district, NW Kyushu, Japan. *Geosci. Repts.* 40, 21–32.

432 Jackson, M., and Bowles, J.A. (2014) Curie temperatures of titanomagnetite in ignimbrites: Effects
433 of emplacement temperatures, cooling rates, exsolution, and cation ordering, *Geochemistry, Geophysics,*
434 *Geosystems* 15, 4343–4368, doi:10.1002/2014GC005527.

435 Jang, Y.D., Naslund, H.R., and McBirney, A.R. (2001) The differentiation trend of the Skaergaard
436 intrusion and the timing of magnetite crystallization: iron enrichment revisited. *Earth and Planetary*
437 *Science Letters*, 189:189–196.

438 Kirkpatrick, R.J. (1983) Theory of nucleation in silicate melts. *American Mineralogist*, 68, 66–77.

439 Kissell, C., Laj, C., Sigurdsson, H., and Guillou, H. (2010) Emplacement of magma in Eastern
440 Iceland dikes. Insights from magnetite fabric and rock magnetic analysis. *Journal of Volcanology and*
441 *Geothermal Research*, 191, 79–92.

442 Keller, F., Guillong, M., Geshi, N., Miyakawa, A., and Bachmann, O. (2023) Tracking caldera
443 cycles in the Aso magmatic system – Applications of magnetite composition as a proxy for
444 differentiation. *Journal of Volcanology and Geothermal Research* 436, 107789.

445 Lanzafame, G., Iezzi, G., Mancini, L., Lezzi, F., Mollo, S., and Ferlito, C. (2017) Solidification
446 and turbulence (non-laminar) during magma ascent: insights from 2D and 3D analyses of bubbles and
447 minerals in an Etnean dyke. *Journal of Petrology* 58 (8), 1511-1533.

448 Lasaga, A.C. (1998) *Kinetic Theory in the Earth Sciences*. Princeton University Press, Princeton,
449 New York.

450 Lattard, D., Engelmann, R., Kontny, A., and Sauerzapf, U. (2006) Curie temperatures of synthetic
451 titanomagnetites in the Fe-Ti-O system. Reassessment of some methodological and crystal chemical
452 effects. *Journal of Geophysical Research*, 111:B12S28.

453 Lofgren, G.E., Huss, G.R., and Wasserburg, G.J. (2006) An experimental study of trace-element
454 partitioning between Ti-Al-clinopyroxene and melt: equilibrium and kinetic effects including sector
455 zoning. *American Mineralogist* 91:1596–1606.

456 McCarthy, A., Chelle-Michou, C., Blundy, J.D., Dorais, M.J., van der Zwan, F.M., and Peate, D.W.
457 (2023) The effect of variations in cooling rates on mineral compositions in mid-ocean ridge basalts.
458 *Chemical Geology*, 625, 121415. [10.1016/j.chemgeo.2023.121415](https://doi.org/10.1016/j.chemgeo.2023.121415).

459 Mollo, S., Lanzafame, G., Masotta, M., Iezzi, G., Ferlito, C., and Scarlato, P. (2011) Cooling
460 history of a dike as revealed by mineral chemistry: A case study from Mt. Etna volcano. *Chemical*
461 *Geology* 2011, 288, 39–52.

462 Mollo, S., Putirka, K., Iezzi, G., and Scarlato, P. (2013) The control of cooling rate on
463 titanomagnetite composition: implications for a geospeedometry model applicable to alkaline rocks from
464 Mt. Etna volcano. *Contributions to Mineralogy and Petrology* 165, 457–475.
465 <https://doi.org/10.1007/s00410-012-0817-6>.

466 Mollo, S., Giacomoni, P.P., Coltorti, M., Ferlito, C., Iezzi, G., and Scarlato, P. (2015)
467 Reconstruction of magmatic variables governing recent Etnean eruptions: Constraints from mineral
468 chemistry and P–T– f_{O_2} –H₂O modelling. *Lithos* 212–215, 311–320.

469 Mollo, S., and Hammer, J.E. (2017) Dynamic crystallization in magmas. In: EMU Notes in
470 Mineralogy, 16, pp. 373–418. <https://doi.org/10.1180/EMU-notes.16.12>.

471 Muncill, G.E., and Lasaga, A.C. (1987) Crystal-growth kinetics of plagioclase in igneous systems:
472 one atmosphere experiments and approximation of a simplified growth model. American Mineralogist
473 72, 299–311.

474 Nadoll, P., Angerer, T., Mauk, J.L., French, D., and Walshe, J. (2014) The chemistry of
475 hydrothermal magnetite: A review. Ore Geology Reviews 61, 1–32.

476 Nikolaev, G.S., Ariskin, A.A. and Barmina, G.S. (2018a) SPINMELT-2.0: Simulation of spinel–
477 melt equilibrium in basaltic systems under pressures up to 15 kbar: I. model formulation, calibration, and
478 tests. Geochemistry International 56, 24–45.

479 Nikolaev, G.S., Ariskin, A.A. and Barmina, G.S. (2018b) SPINMELT-2.0: Simulation of spinel–
480 melt equilibrium in basaltic systems under pressures up to 15 Kbar: II. Description of the program
481 package, the topology of the Cr-spinel–melt model system, and petrological implications. Geochemistry
482 International 56, 125–135.

483 O'Reilly W. (1984) Rock and mineral magnetism. Blackie, Glasgow, p 220.

484 Mysen, B.O., and Richet, P. (2005) Silicate glasses and melts: properties and structure.
485 Developments in geochemistry, vol 10. Elsevier, Amsterdam, p 544.

486 Pauling, L. (1960) The Nature of the Chemical Bond—An Introduction to Modern Structural
487 Chemistry. 3rd Edition, Cornell University Press, Ithaca, New York, 10-13.

488 Pick, T., and Tauxe, L. (1994) Characteristics of magnetite in submarine basaltic glass.
489 Geophysical Journal International 119:116–128.

490 Pontesilli, A. Masotta, M., Nazzari, M., Mollo, S., Armienti, P., Scarlato, P., and Brenna, M. (2019)
491 Crystallization kinetics of clinopyroxene and titanomagnetite growing from a trachybasaltic melt: New
492 insights from isothermal time-series experiments. Chemical Geology, 510, 113–129.

493 Roskosz, M., Toplis, M.J., Besson, P., and Richet, P. (2005) Nucleation mechanisms: a crystal
494 chemical investigation of phases forming in highly supercooled aluminosilicate liquids. *Journal of Non-*
495 *Crystalline Solids* 351, 1266–1282.

496 Roskosz, M., Toplis, M.J., and Richet, P. (2006) Kinetic vs. thermodynamic control of nucleation
497 and growth in molten silicates. *Journal of Non-Crystalline Solids* 352, 180–184.

498 Scaillet, B., and Evans, B.W. (1999) The 15 June 1991 eruption of Mount Pinatubo. I. Phase
499 equilibria and pre-eruption P-T-fO₂-fH₂O conditions of the dacite magma. *Journal of Petrology* 40:381–
500 411.

501 Smith, B.M., and Prévot, M. (1977). Variation of the magnetic properties in a basaltic dyke with
502 concentric cooling zones. *Physics of the Earth and Planetary Interiors* 14, 120–136.

503 Smith, P.M., and Asimow, P.D. (2005) Adiaabat_1ph: a new public front-end to the MELTS,
504 pMELTS, and pHMELTS models. *Geochemistry, Geophysics, Geosystems* 6, Q02004.
505 <https://doi.org/10.1029/2004GC000816>.

506 Stormer, J.C. Jr. (1983) The effects of recalculation on estimates of temperature and oxygen
507 fugacity from analyses of multicomponent iron-titanium oxides. *American Mineralogist* 68:586–594.

508 Toplis, M.J., and Carroll, M.R. (1995) An experimental study of the influence of oxygen fugacity
509 on Fe–Ti oxide stability, phase relations, and mineral-melt equilibria in ferro-basaltic systems. *Journal*
510 *of Petrology* 36, 1137–1170.

511 Vetere, F., Behrens, H., Holtz, F., Neuville, D.R. (2006) Viscosity of andesitic melts – new
512 experimental data and a revised calculation model. *Chemical Geology* 228, 233-245.

513 Vetere, F., Iezzi, G., Perugini, D. and Holtz, F. (2022) Rheological Changes in Melt and Magma
514 Induced by Deformation and Cooling Events. *CR-Geosciences*, 354, p. 1-22.
515 <https://doi.org/10.5802/crgeos.125>

516 Vetere, F., Iezzi, G., Beherens, H., Holtz, F., Ventura, G., Misiti, V., Cavallo, A., Mollo, S., and
517 Dietrich, M. (2015) Glass forming ability and crystallization behaviour of sub – alkaline silicate melts.
518 Earth-Science Reviews 150, 25–44.

519 Vetere, F., Iezzi, G., Beherens, H., Cavallo, A., Misiti, V., Dietrich, M., Knipping, J., Ventura, G.,
520 and Mollo, S. (2013) Intrinsic solidification behaviour of basaltic to rhyolitic melts: a cooling rate
521 experimental study. Chemical Geology 354, 233–242.

522 Zhang, Y., Walker, D., and Leshner, C.E. (1989) Diffusive crystal dissolution. Contribution to
523 Mineralogy and Petrology 102, 492–513.

524 Zhang, Y. (2008) Geochemical Kinetic. Princeton University Press, New York.

525 Zhang, W., Zeng, Z., Cui, L., and Yin, X. (2018) Geochemical constraints on MOBR composition
526 and magma sources at East Pacific rise between 1°S and 2°S. Journal of Ocean University of China
527 (Oceanic and Coastal Sea Research) 17 (2), 297–304.

528 Zhao, Q., Yan, Z., Chen, C., and Chen, J. (2017) Spinels: Controlled Preparation, Oxygen
529 Reduction/Evolution Reaction Application, and Beyond. Chemical Reviews, 117: 10121–10211. DOI:
530 10.1021/acs.chemrev.7b00051.

531 Zhao, L., Chen, H., Zhang, L., Li, D., Zhang, W., Wang, C., Yang, J., and Yan, X. (2018) Magnetite
532 geochemistry of the Heijianshan Fe-Cu (-Au) deposit in Easter Tianshan: Metallogenic implications for
533 submarine volcanic-hosted Fe-Cu deposits in NW China. Ore Geology Reviews, 100, 422-440.

534 Zhou, W., Van der Voo, R., Peacor, D.R., and Zhang, Y. (2000) Variable Ti-content and grain size
535 of titanomagnetite as a function of cooling rate in very young MORB. Earth and Planetary Science Letters
536 179, 9–20.

537 Xu, Z.-H., Yang, Z.-F., An, X.-H., Xu, R., and Qi, J.-N. (2022) Relationship between the Texture
538 and Composition of Titanomagnetite in Hannuoba Alkaline Basalt: A New Geospeedometer. Minerals
539 2022, 12, 1412. <https://doi.org/10.3390/min12111412>.

List of figure captions

Figure 1. X-ray EPMA-WDS maps of the distribution of SiO₂, TiO₂, Al₂O₃, FeO^{tot} (two ranges), MgO CaO and Na₂O, plus the textural features by back-scattered SEM micro-photographs (top). The changes from blue to red colors indicate an increasing for each oxide wt% range. The horizontal white (black) bars correspond to 100 μm.

Figure 2. Major oxides (wt%) in spinel as function of FeO^{tot} and number of selected EPMA-WDS analyses. The TiO₂, Al₂O₃, FeO^{tot} (Fe₂O₃ in Giuliani et al., 2022) ranges obtained by single-selected EPMA points are all comprised in the corresponding ranges measured here, whereas only some of the MgO data analysis presented in Giuliani et al., (2022) are higher than the maximum value measured here (up to ~ 20 wt.%).

Figure 3. Abundances of cations (apfu) in spinel as function of Fe³⁺ content and number of selected EPMA-WDS analyses. Red star symbols represent the theoretical composition of spinel as computed by alphaselms 1.9 (Asimow and Ghiorso, 1998; Ghiorso et al., 2002; Smith and Asimow, 2005; Giuliani et al., 2022).

Figure 4. Distribution of cations (apfu) in spinel (Sp) calculated from the data in Figure 3, as a function of cooling rate.

Figure 5. Ternary plot showing the average Usp (ulvospinel), Mt (magnetite), Sp s.s. (spinel sensu stricto) molecular components in spinel as determined in this study with X-ray EPMA maps and in the previous one (Giuliani et al., 2022) that used the classical set of single EPMA analytical points.

Figure 6. Average of cations (apfu) in spinel as function of the cooling rate (°C/h). Mg²⁺+Fe²⁺ and Al³⁺+Fe³⁺ sum are also shown. Only linear regression with R² > 0.6 are plotted. Red symbols in some plots represent the average cations of spinel from Giuliani et al. (2022).

Figure 7. Ternary plot showing the distribution of average amounts of Ti^{4+} , $Al^{3+} + Fe^{3+}$ and $Mg^{2+} + Fe^{2+}$ cations in spinel.

Table 1. Experimental conditions of solidification experiments, phase assemblages and analytical EPMA-WDS features.

sample label	cooling rate (°C/h)	crystal content	map area (mm ²)	distance between adjacent analytical points (µm)	number of reliable single analytical points
E1	1	Plg+Px+Sp	0.68	1.65	902
E7	7	Plg+Px+Sp	1.00	2.0	993
E60	60	Plg+Px+Sp	0.25	1.0	133
E180	180	Px+Sp+glass	0.25	1.0	24

footnote: Plg=plagioclase, Px=pyroxene, Sp= spinel

Table 2. Average contents of oxides, cations and molecules in spinel.

# selected analyses	E1 (n=902)		E7 (n=994)		E60 (n=133)		E180 (n=24)	
	av.	σ	av.	σ	av.	σ	av.	σ
oxide (wt%)								
SiO ₂	0.37	0.37	0.33	0.37	0.53	0.52	0.44	0.39
TiO ₂	4.34	4.01	4.06	3.03	2.22	1.26	0.49	0.28
Al ₂ O ₃	2.86	1.90	3.41	1.64	8.93	2.50	9.26	1.12
FeO ^{tot}	78.31	4.58	73.50	3.05	72.67	3.32	67.47	1.97
MgO	7.73	4.48	11.11	2.78	7.94	1.74	12.92	1.39
CaO	0.13	0.26	0.13	0.26	0.38	0.29	0.24	0.28
MnO	0.61	0.48	0.93	0.53	0.46	0.33	0.43	0.34
tot.	94.36	2.94	93.46	2.45	93.13	1.67	91.44	1.43
cations (apfu)								
Si ⁴⁺	0.01	0.01	0.01	0.01	0.02	0.02	0.02	0.01
Ti ⁴⁺	0.12	0.11	0.11	0.08	0.06	0.04	0.01	0.01
Al ³⁺	0.12	0.08	0.14	0.06	0.36	0.10	0.37	0.04
Fe ³⁺	1.62	0.19	1.62	0.16	1.48	0.07	1.57	0.06
Fe ²⁺	0.71	0.34	0.51	0.22	0.64	0.11	0.35	0.06
Mg ²⁺	0.40	0.22	0.57	0.14	0.41	0.08	0.66	0.06
Mn ²⁺	0.02	0.01	0.03	0.02	0.01	0.01	0.01	0.01
Fe ²⁺ /Fe ³⁺	0.44		0.31		0.43		0.22	
components (mol%)								
Sp s.s.	17.48	9.39	24.05	5.78	26.24	5.54	34.68	2.07
Mt	62.55	3.45	60.63	3.31	57.34	2.71	57.02	1.62
Usp	19.96	11.20	15.32	7.70	16.42	3.65	8.30	1.32

footnote: Sp= spinel sensu stricto, Mt=magnetite, Usp=Ulvospinel

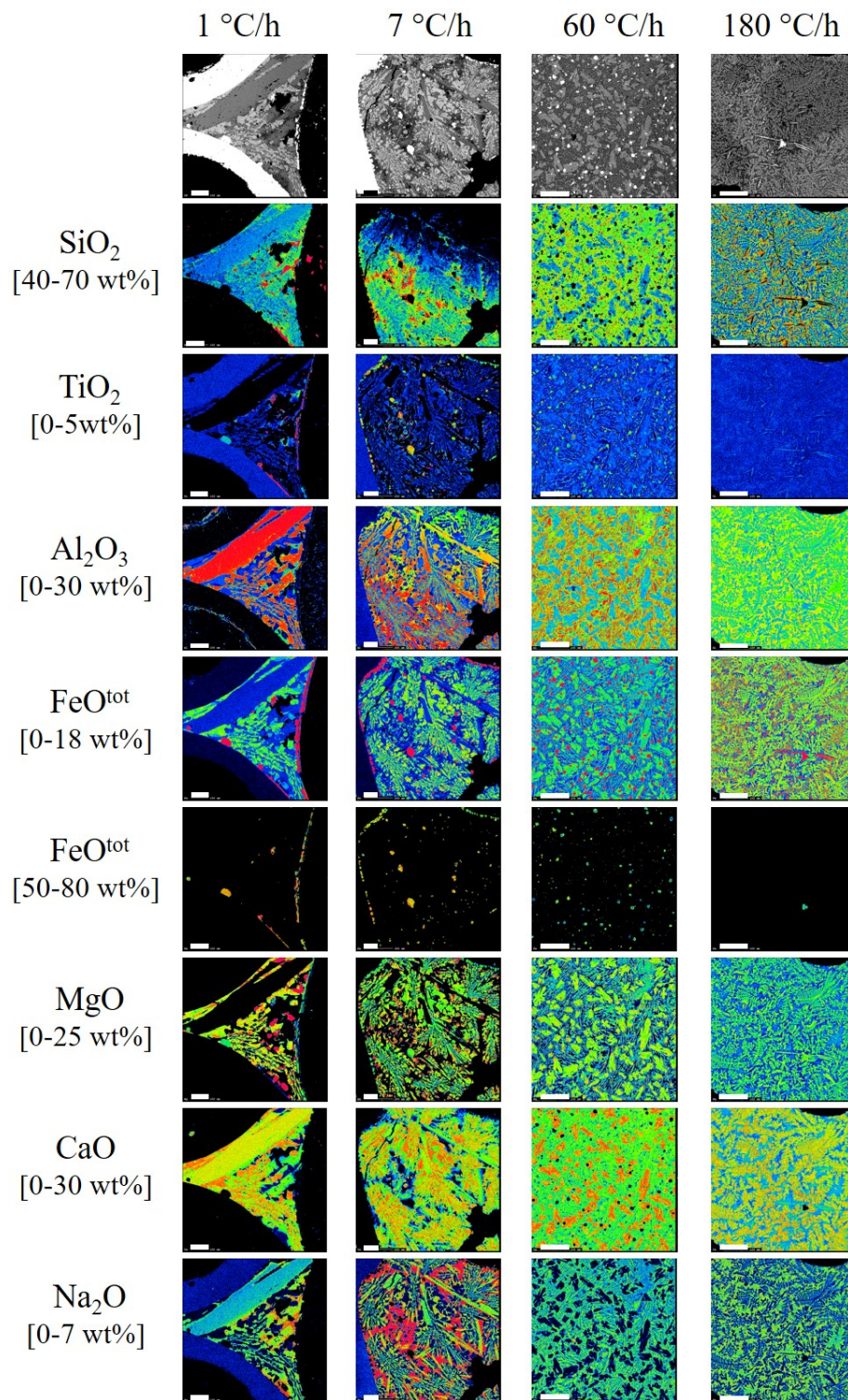


Figure 1

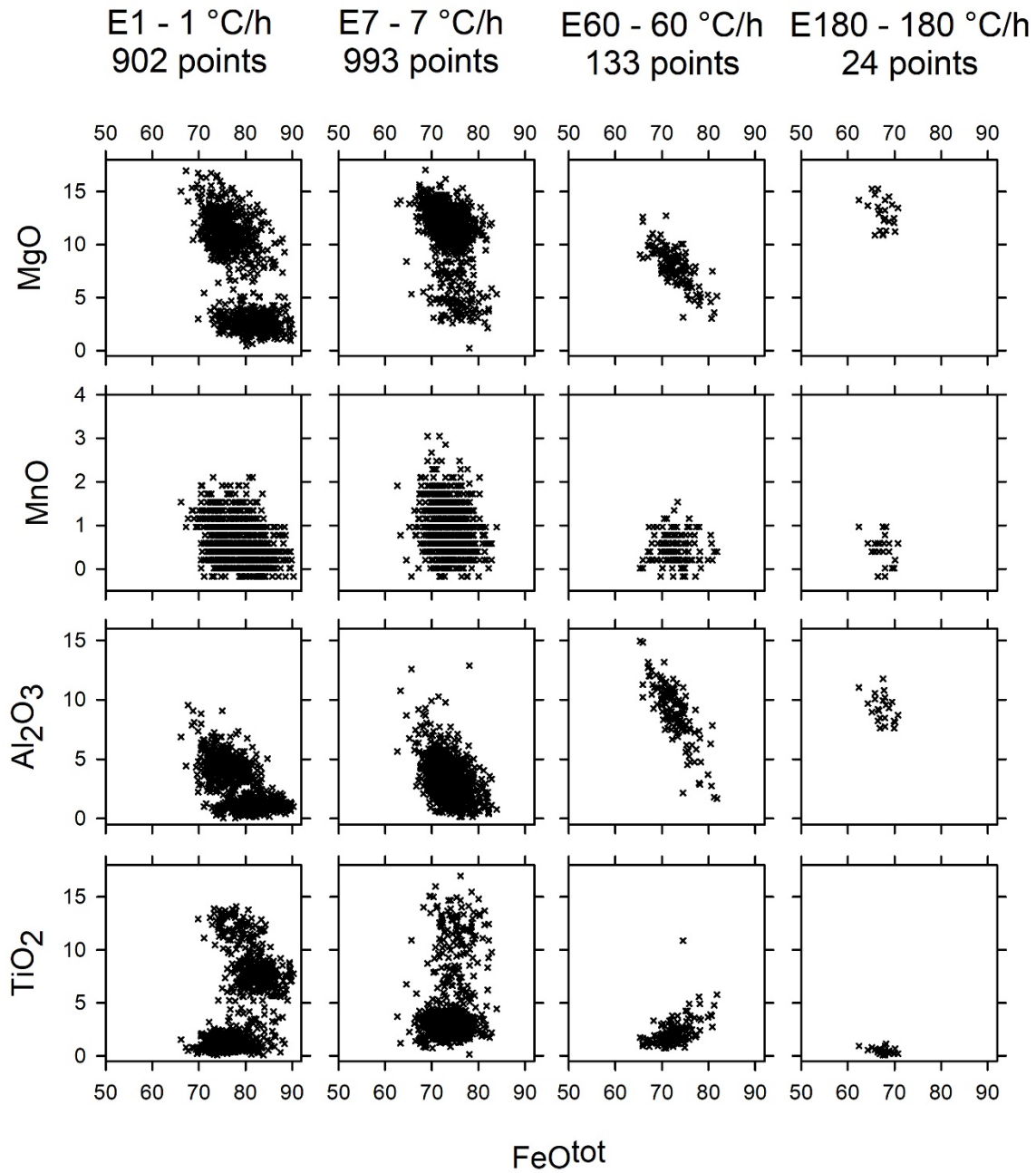


Figure 2

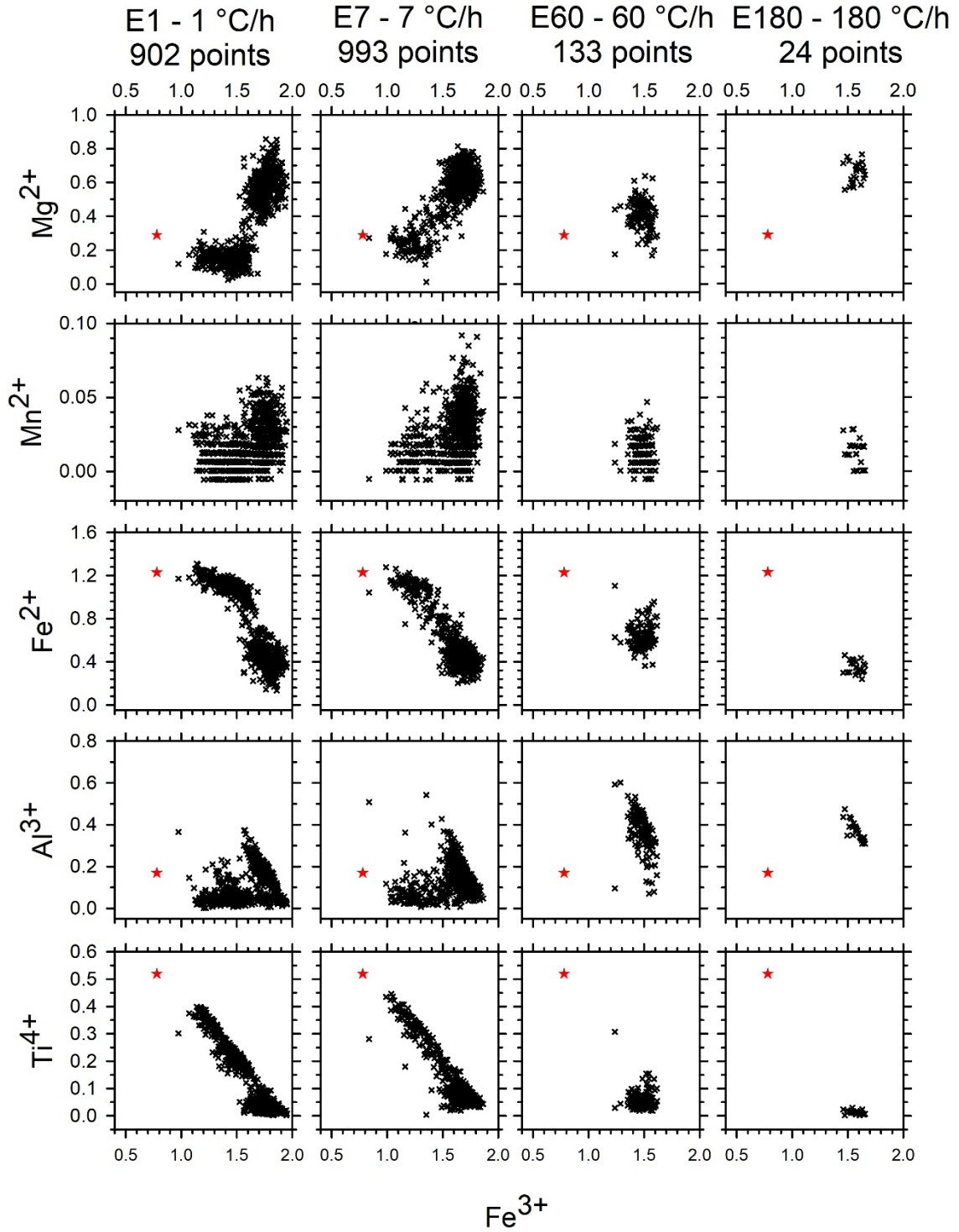


Figure 3

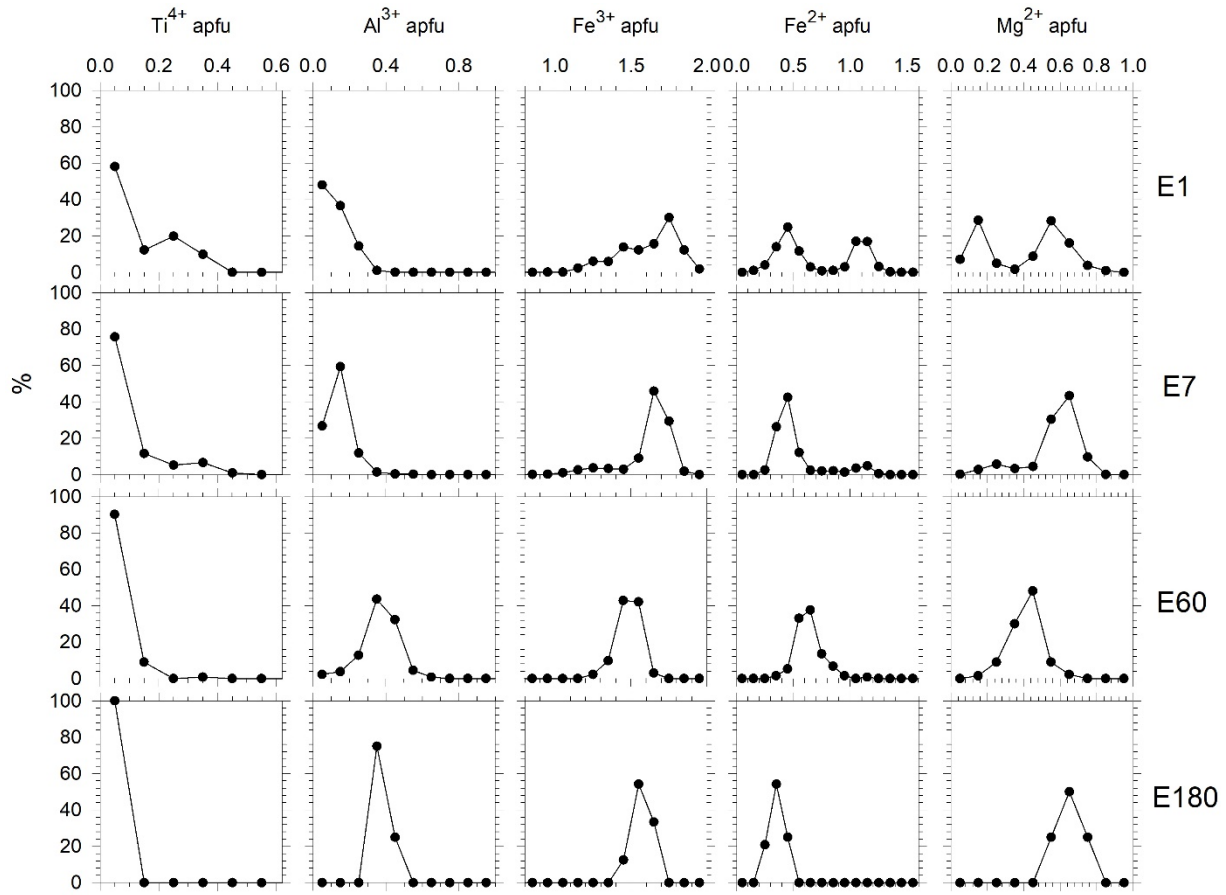


Figure 4

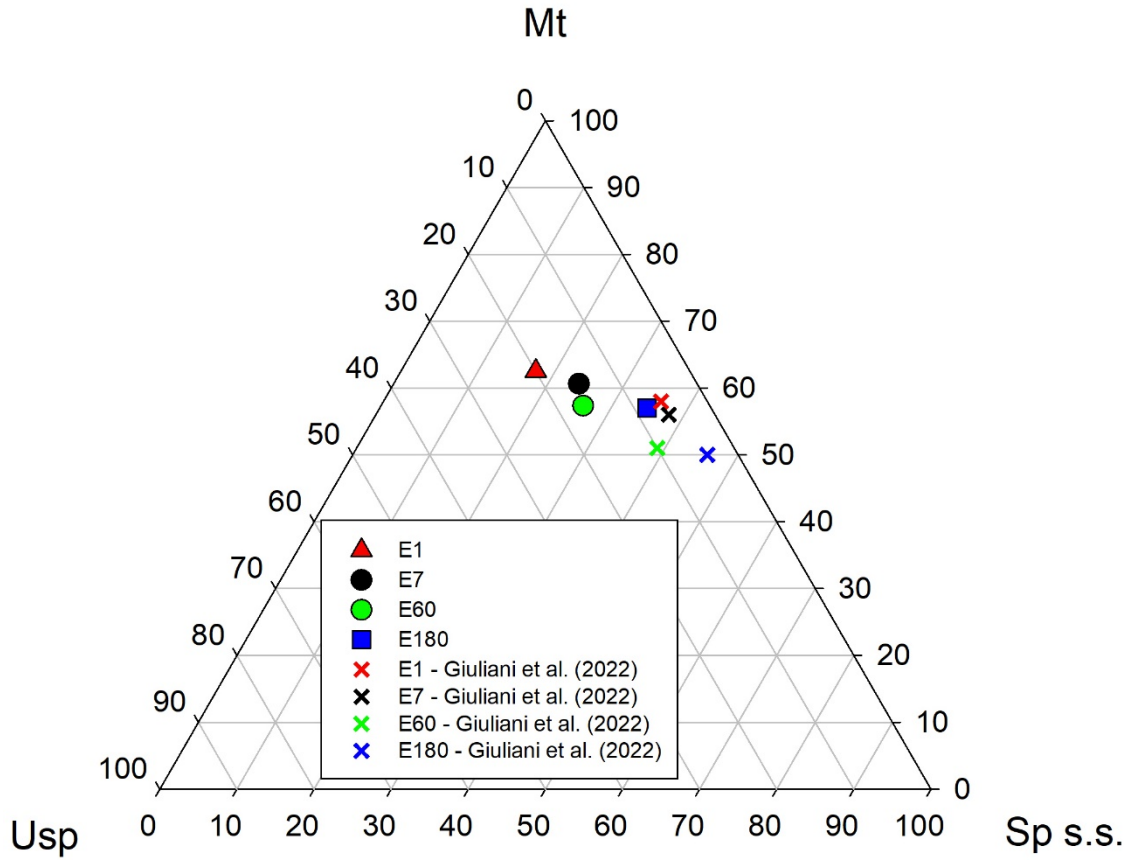


Figure 5

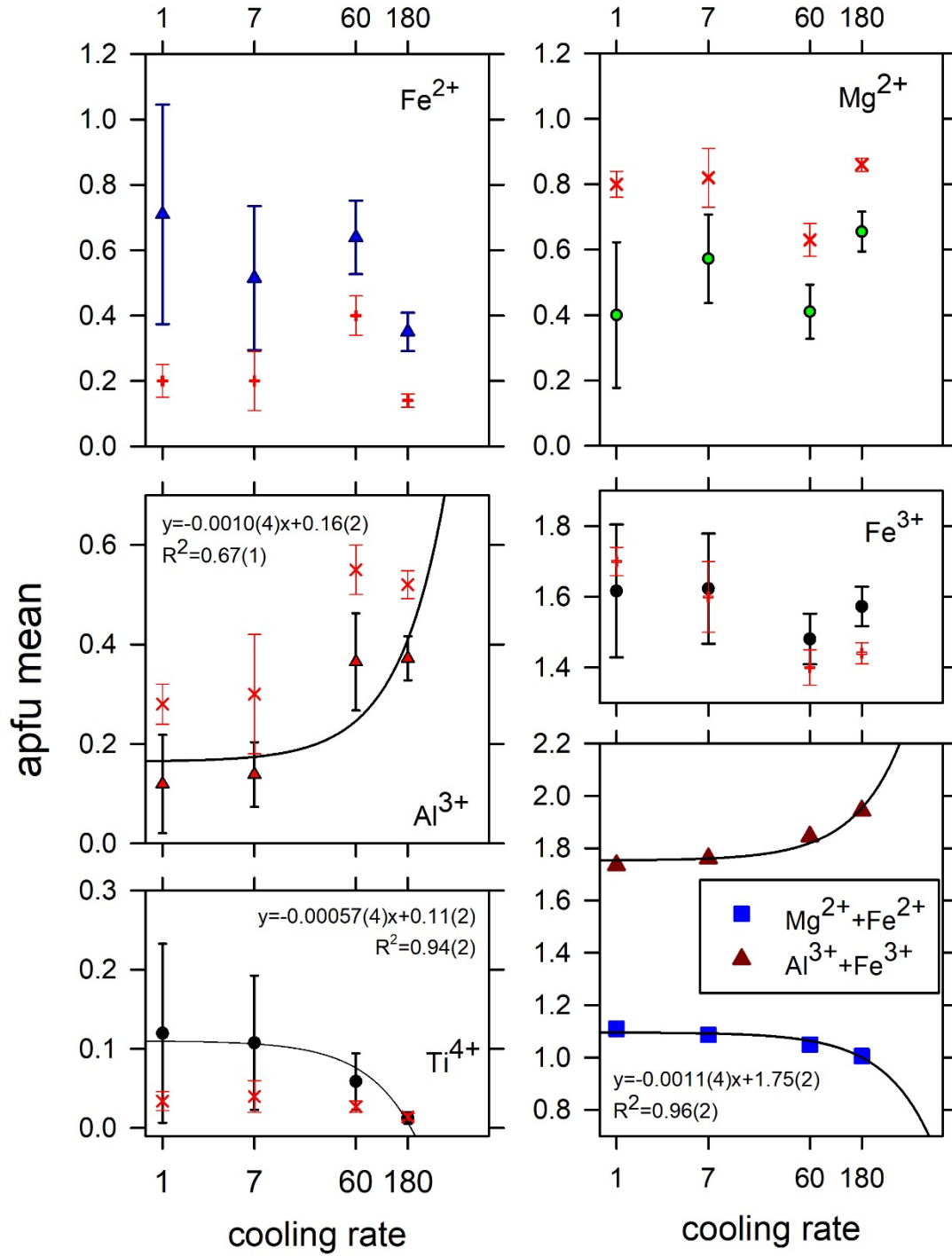


Figure 6

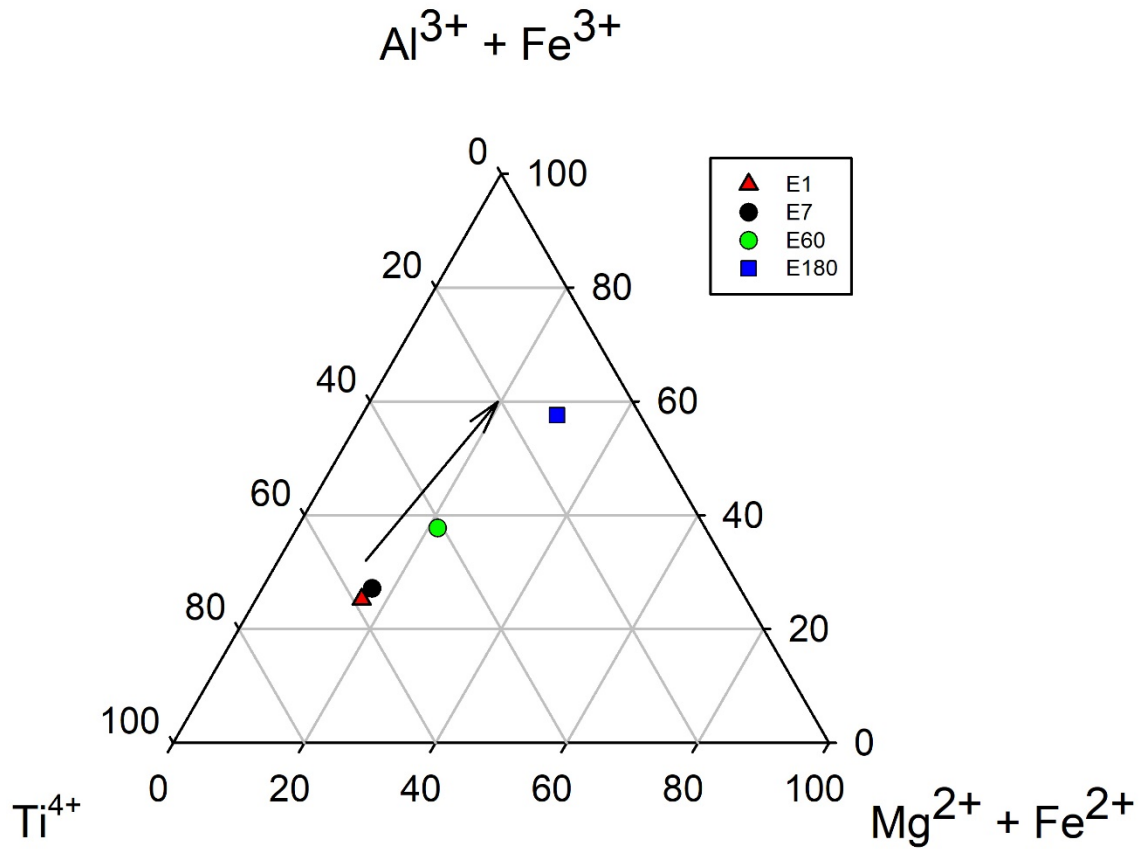


Figure 7